Materials Horizons

ROYAL SOCIETY OF CHEMISTRY

COMMUNICATION

View Article Online
View Journal | View Issue

Published on 30 August 2023. Downloaded by East China Normal University on 10/31/2023 1:35:46 AM.

Cite this: *Mater. Horiz.*, 2023, **10**, 5099

Received 18th July 2023,
Accepted 25th August 2023

DOI: 10.1039/d3mh01120h

rsc.li/materials-horizons

A polar-switchable and controllable negative phototransistor for information encryption

Aiping Cao,[a] Shubing Li,[a] Hongli Chen,[a] Menghan Deng,[a] Xionghu Xu,[a] Liyan Shang,[a] Yawei Li,[a] Anyang Cui[b] and Zhigao Hu*[ac]

Anomalous negative phototransistors have emerged as a distinct research area, characterized by a decrease in channel current under light illumination. Recently, their potential applications have been expanded beyond photodetection. Despite the considerable attention given to negative phototransistors, negative photoconductance (NPC) in particular remains relatively unexplored, with limited research advancements as compared to well-established positive phototransistors. In this study, we designed ferroelectric field-effect transistors (FeFETs) based on the WSe_2/CIPS van der Waals (vdW) vertical heterostructures with a buried-gated architecture. The transistor exhibits NPC and positive photoconductance (PPC), demonstrating the significant role of ferroelectric polarization in the distinctive photoresponse. The observed inverse photoconductance can be attributed to the dynamic switching of ferroelectric polarization and interfacial charge transfer processes, which have been investigated experimentally and theoretically using Density Functional Theory (DFT). The unique phenomena enable the coexistence of controllable and polarity-switchable PPC and NPC. The novel feature holds tremendous potential for applications in optical encryption, where the specific gate voltages and light can serve as universal keys to achieve modulation of conductivity. The ability to manipulate conductivity in response to optical stimuli opens up new avenues for developing secure communication systems and data storage technologies. Harnessing this feature enables the design of advanced encryption schemes that rely on the unique properties of our material system. The study not only advances the development of NPC but also paves the way for more robust and efficient methods of optical encryption, ensuring the confidentiality and integrity of critical information in various domains, including data transmission, and information security.

New concepts

The work proposes a novel information security approach through the design of a nonvolatile transistor using a two-dimensional (2D) WSe_2/CIPS heterostructure. Our method exploits the coupling of built-in electric field and ferroelectric polarization in the WSe_2/CIPS heterojunction to efficiently manipulate photogenerated carriers, enabling coexistence of controlled and switchable positive and negative photoconductivity in a single device. The unique switchable photoelectronic effect of WSe_2/CIPS heterostructure has been visualized *in situ* using the conductive atomic force microscope (C-AFM) system. Moreover, signal recovery and decryption can be achievable by controlling the light switch, establishing a switchable and controllable optical encryption function. These groundbreaking findings elucidate the negative photoconductance of 2D ferroelectric materials and facilitate the development of an optical encryption device, enhancing our understanding of negative photoconductance effects on 2D optoelectronics.

Conceptual insights

Traditional encryption methods involving hardware integration into chip designs lead to increased complexity. The study proposes a novel information security approach through the design of a nonvolatile transistor using a two-dimensional (2D) WSe_2/CIPS heterostructure. Our method exploits the coupling of built-in electric field and ferroelectric polarization in the WSe_2/CIPS heterojunction to efficiently manipulate photogenerated carriers, enabling coexistence of controlled and switchable PPC and NPC in a single device. The unique switchable photoelectronic effect of WSe_2/CIPS heterostructure has been visualized *in situ* using the conductive atomic force microscope (C-AFM) system. Utilizing a specific gate voltage and laser as the

[a] Technical Center for Multifunctional Magneto-Optical Spectroscopy (Shanghai), Engineering Research Center of Nanophotonics & Advanced Instrument (Ministry of Education), Department of Physics, School of Physics and Electronic Science, East China Normal University, Shanghai 200241, China. E-mail: zghu@ee.ecnu.edu.cn; Fax: +86-21-54342933; Tel: +86-21-54345150
[b] Key Laboratory of Optoelectronic Material and Device, Department of Physics, Shanghai Normal University, Shanghai 200234, China
[c] Collaborative Innovation Center of Extreme Optics, Shanxi University, Taiyuan, Shanxi 030006, China

This journal is © The Royal Society of Chemistry 2023

encryption key, a novel optical encryption device has been realized. Moreover, signal recovery and decryption can be achievable by controlling the light switch, establishing a switchable and controllable optical encryption function. These groundbreaking findings elucidate the negative photoconductance of 2D ferroelectric materials and facilitate the development of an optical encryption device, enhancing our understanding of negative photoconductance effects on 2D optoelectronics.

Published on 30 August 2023. Downloaded by East China Normal University on 10/31/2023 1:35:46 AM.

1 Introduction

Ultrathin films of layered materials have captured considerable attention because of their fascinating physical properties that vary with reduced thickness, which in recent years have been shown to be promising for a bewildering variety of applications to photonic and optoelectronic devices. Typically, electronic state regulation can be achieved through chemical doping or traditional dielectrics, but these methods can introduce defects, disorder, reducing carrier mobility and FET structures require external gate voltage to maintain doping, which is not suitable for low-power devices. A non-defect-free and non-volatile strategy is needed, and ferroelectric grid field regulation can provide this solution. The FeFET is recognized as an attractive architecture for photodetectors devices due to its nondestructive operation and nonvolatility. The development of 2D van der Waals ferroelectrics could lead to the next technological breakthrough in the post-Moore era. Up to now, a few materials have been reported to maintain the ferroelectricity in ultrathin films at room temperature, such as $CuInP_2S_6$ (CIPS), In_2Se_3, WTe_2, and $MoTe_2$.[1–5] Among these 2D ferroelectric materials, the representative CIPS with non-volatile and room-temperature ferroelectric properties make it an ideal candidate for constructing vertical heterojunction phototransistors. This innovative approach promises to yield phototransistors with superior optoelectronic properties.[6–9] Additionally, the non-volatile storage capabilities of CIPS offer the advantage of tunability, further enhancing its potential applications in this field.

Recently, various inorganic (black phosphorus, MoS_2, InAs NWs),[10–13] organic (C8-BTBT, TFT-CN, GQDs),[14,15] and perovskite materials[16,17] have been reported to present an unusual NPC. The remarkable characteristic of NPC is characterized by a significant drop in the conductivity of semiconductors once it is illuminated. The development of NPC is highly desirable for the advancement of innovative optoelectronic applications. The NPC phenomena have the potential to provide optoelectronic devices with high-speed frequency response and low power consumption. Furthermore, when combined with PPC, NPC acts as a complementary component, expanding the functionality of conventional optoelectronic devices and enabling the construction of multifunctional optoelectronic devices.[18–23] However, it should be noted that the reported origin of NPC phenomena is influenced by various external factors, such as temperature, humidity, defect concentration.[24] All these factors exhibit instability and a lack of controllability, posing challenges in achieving precise and controllable NPC and PPC performance within a single sample.

Herein, we design a nonvolatile transistor based on a 2D WSe_2/CIPS heterostructure and systematically study the tunable photoresponse under illumination, where the negative preset polarization gives rise to PPC, whereas the positive preset polarization leads to NPC. The analysis assisted with the various experiments and DFT indicates that the fascinating phenomenon can be attributed to the coupling of built-in electric field with ferroelectric polarization, which enables the photogenerated carriers in WSe_2 to efficiently migrate and recombine at the heterojunction interface. Since 2D ferroelectric materials have non-volatile polarization, the presence of non-volatile polarization in 2D ferroelectric materials allows direct manipulation of the built-in electric field without the continuous application of additional gate voltage. This not only simplifies device complexity but also reduces power consumption while improving device performance. By controlling the nonvolatile polarization of 2D ferroelectric materials, we achieve modulation of the optoelectronic properties of the device. Furthermore, we explore the potential application of the 2D WSe_2/CIPS heterostructure in multilevel information encryption based on the tunable photoresponse properties. This strategy opens avenues for the development of secure protection of confidential information.

2 Results and discussion

2.1 Characterization of WSe_2/CIPS Heterostructure

Fig. 1a presents a schematic diagram of the WSe_2/CIPS 2D heterostructure FeFET, where the layered CIPS is used as the ferroelectric gate dielectric layer and WSe_2 is used as light-sensitive layer. The patterned Cr/Au (2 nm/50 nm) layers are deposited as the source, drain and gate electrodes by thermal evaporation. The bottom-gate are labeled as ‘‘buried-gate electrode’’. The optical and topographic images of a typical device are displayed in Fig. 1b and c, respectively. The thickness of the CIPS nanoflakes is about 75 nm, and the thickness of the WSe_2 film is about 1.7 nm, corresponding to two molecular layers. It is worth mentioning that CIPS is a two-dimensional ferroelectric material, which imparts excellent insulating properties[5] and allows for the modulation of the channel conductivity through its ferroelectric polarization. This material effectively separates the gate electrode from the semiconductor channel and enables the control of the transistor's operation. Meanwhile, the polarization introduces an electric field that penetrates the entire CIPS layer, influencing the adjacent WSe_2 semiconductor layer. Even though the ferroelectric interface is distant from the gate electrode, this electric field manages to permeate into the WSe_2 layer. Within the path of the source-drain current, the carrier density of WSe_2 is modulated by this electric field, thus influencing the magnitude of the source-drain current. By precisely controlling the ferroelectric nonvolatile polarization, the optoelectronic properties of the transistor can be modulated. Additional details on the interlayer coupling of the vdW heterostructure could be found from Raman spectra. Fig. 1d illustrates the Raman spectrum of an exfoliated CIPS, WSe_2 nanoflakes and

 This journal is © The Royal Society of Chemistry 2023

Published on 30 August 2023. Downloaded by East China Normal University on 10/31/2023 1:35:46 AM.

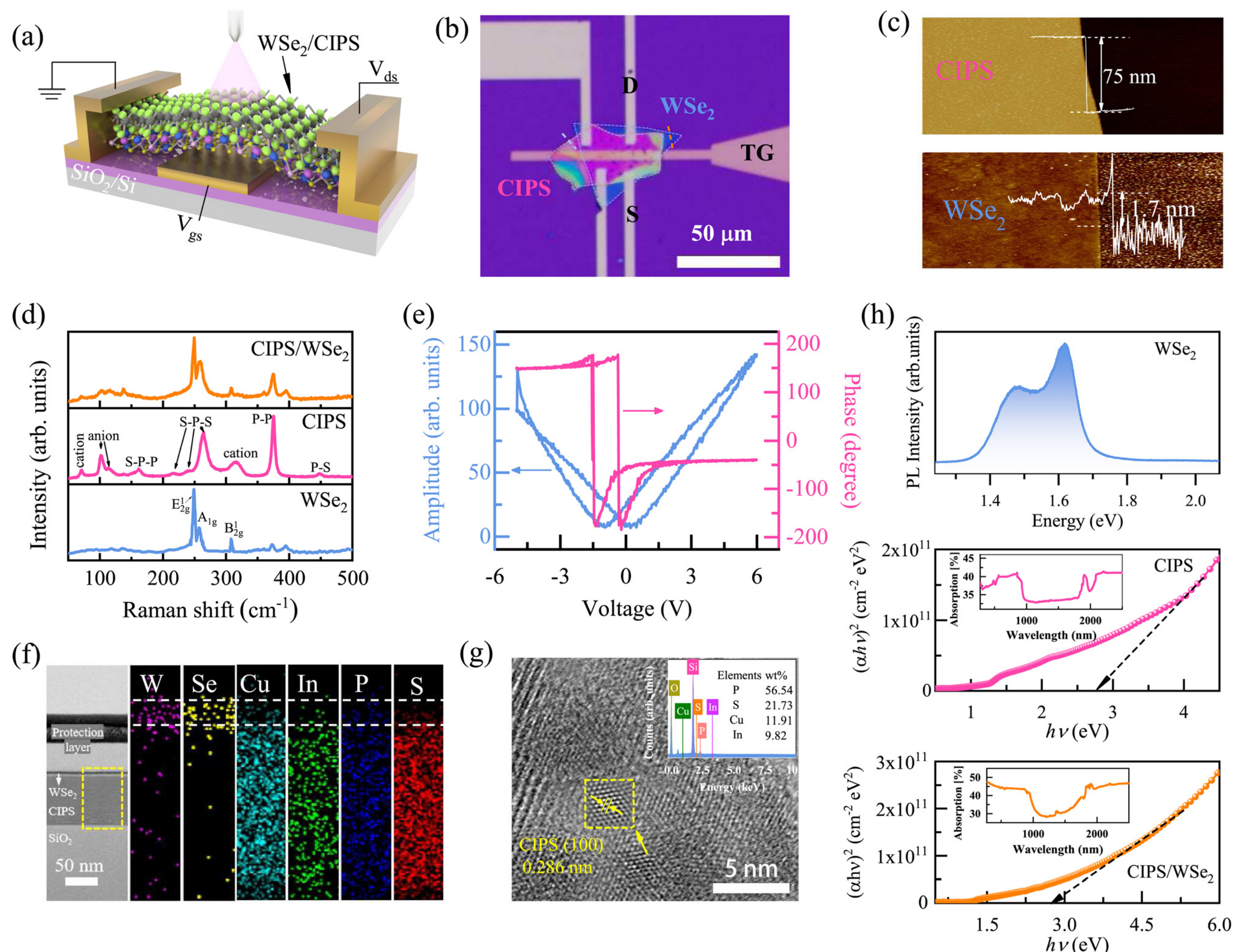

Fig. 1 (a) Schematic view of a FeFET based on a WSe_2/CIPS heterostructure. (b) An optical image of a WSe_2/CIPS heterostructure device fabricated on a SiO_2/Si substrate, where the scale bar is 50 μm. (c) AFM topography of the 75 nm thick CIPS nanoflakes and 1.7 nm thick WSe_2 upon the substrate. The inset is height profile along the orange and blue dashed dashed line in (b). (d) Corresponding Raman spectra of the CIPS, WSe_2 nanoflakes and CIPS/WSe_2 heterostructure, respectively. (e) Out-of-plane amplitude and phase measurements of CIPS nanoflakes *versus* voltage obtained by PFM on Pt/SiO_2/Si substrate. (f) Cross-sectional TEM image and corresponding EDS element mapping of WSe_2/CIPS heterostructure. (g) High-resolution TEM images and EDS spectrum (inset) of CIPS nanoflakes. (h) The band gap characterization of WSe_2, CIPS, and WSe_2/CIPS heterostructure achieved through photoluminescence spectrum (PL) (up), and absorption spectra (middle, down), and curve of $(\alpha h\nu)^2$ *vs.* photon energy obtained from the absorption spectra data.

WSe_2/CIPS heterostructure at room temperature, respectively. Raman spectra recorded match well with the previous reports on WSe_2.[25] The as-exfoliated WSe_2 film shows three distinct peaks observed at ∼249.1, ∼257.5, and ∼308.5 cm^{-1}, which correspond to the A_{1g}, E^1_{2g}, and B^1_{2g} Raman-active modes of the bilayers WSe_2, respectively.

The locations of the Raman peaks from the exfoliated CIPS flakes also showed the same characteristics as previous reported vibration modes in bulk CIPS crystals at ferroelectric phase.[26] Three dominant peaks are observed in the ∼71.3, 90–140, and ∼316.6 cm^{-1} ranges, which are responsible for the vibrational modes of cation (Cu^I, In^{III}) and anion ($P_2S_6{}^{4-}$), respectively. After the formation of WSe_2/CIPS heterostructure, the vibrational peaks of WSe_2 were mingled with those of CIPS. It was found that the vibrational mode of in-plane E^1_{2g} mode remained almost unchanged, while the out-of-plane A_{1g} mode exhibited a shift in the wavenumber of 3–4 cm^{-1}. This observation results indicate that the oscillator spring can be affected by an extra interlayer interaction term, leading to a stiffening of the A_{1g} vibrational mode.[27] In order to analyze the ferroelectric properties of the CIPS flakes on a Au/SiO_2/Si substrate, we conducted phase and amplitude hysteresis loops using Dual AC Resonance-Tracking Piezoresponse Force Microscope (DART-PFM) at a single point in tapping mode.[26,28–30] Fig. 1e displays the butterfly-like amplitude hysteresis loop and the distinct 180° phase switching under a changing electric field, indicating the existence of ferroelectricity. To gain more insight into the structure of the WSe_2/CIPS heterostructure, cross-sectional transmission electron microscopy (TEM) investigation was performed, as shown in Fig. 1f. Energy Dispersive

Published on 30 August 2023. Downloaded by East China Normal University on 10/31/2023 1:35:46 AM.

Spectroscopy (EDS) elemental mappings on W, Se, Cu, In, P, and S at the yellow square area in Fig. 1f prove the formation of WSe_2/CIPS heterostructure. The corresponding high-resolution TEM (HRTEM) images exhibit a specific lattice spacing of the (100) facet for CIPS measured to be 0.56 nm, as shown in Fig. 1g. The EDS analysis match well with CIPS stoichiometry, as shown in the inset of Fig. 1g (inset).[31] The atomic percent (atom %) of S, P, Cu, and In is 56.5, 21.7, 12.9, and 8.9, respectively. To investigate the band gap and the optical absorption properties of heterojunctions, PL and the UV-Vis absorption spectra of WSe_2, CIPS, and WSe_2/CIPS heterojunction were depicted in Fig. 1h. From the PL peaks in Fig. 1h (up), we can deduce that the band gap of bilayer WSe_2 is about 1.61 eV, which present typical material properties of WSe_2. For CIPS and WSe_2/CIPS heterostructure, the UV-Vis-NIR absorption spectrum demonstrates prominent absorption in the ultraviolet region and a relatively weaker absorption in the visible range. The distinct absorption features in both UV and visible regions collectively contribute to WSe_2/CIPS heterostructure light absorption characteristics. The band gap of CIPS and WSe_2/CIPS heterostructure could be obtained according to the Tauc formula: $(\alpha h\nu)^2 = C(h\nu - E_g)$, where α, $h\nu$, C and E_g are the absorption coefficient, photo energy, a constant and the band gap, respectively. Based on the extrapolation of the linear part of the plot of $(\alpha h\nu)^2$ *vs.* $h\nu$ indicated in Fig. 1h (middle and down), the band gap E_g of CIPS and WSe_2/CIPS heterostructure can be deduced to be 2.87 eV and 2.71 eV.

2.2 Negative photoresponse properties of WSe_2/CIPS heterostructure

CIPS is a ferroelectric semiconductor material with room temperature ferroelectric effect.[32] WSe_2 is a semiconductor with a bandgap ranging from 1.30 eV to 1.63 eV depending on its thickness and ultrahigh photoresponsivity.[33,34] When these two materials form a heterojunction, the difference in their energy bands results in the formation of an internal electric field and charge distribution. To investigate the intrinsic transport properties of WSe_2/CIPS heterostructure, bilayer WSe_2 and CIPS nanoflakes are fabricated into bottom-gate FeFET devices as shown in Fig. 1a.

The representative transfer curve for the devices with vertical alignment is shown in Fig. 2a, which exhibits a typical shift of ambipolar transfer curve under dark.[18] As can be seen from Fig. 2a of red dotted line, the leakage current I_{gs} through the insulator is negligible as compared to the drain current I_{ds}, further confirming the good insulating properties of the CIPS nanoflakes. Moreover, Fig. 2b shows the ability of UV laser to completely suppress gate-induced carriers achieved by turning on the light at the start of the measurement and then promptly turning it off. This presents a promising capability to precisely control the ΔV_{th} of transistors through manipulation of light signals.[18] Fig. 2c–e depict the typical output characteristic curves of the devices under varying laser power densities at V_{gs} = 0 V, V_{gs} = 2 V, and V_{gs} = −2 V, respectively. The experimental results demonstrate a linear relationship between I_{ds} and V_{ds}, indicating that the vertical WSe_2/CIPS heterostructure have an ohmic contact with the Au electrodes.[24] Interestingly, when a positive preset gate voltage (V_{gs} = 2 V) is applied (as indicated by the dashed arrow), a noticeable decrease in I_{ds} caused by the illumination is observed. At a V_{ds} of 1.5 V and an intensity of 7.0 mW cm^{-2}, a negative photocurrent of approximately 0.019 nA is achieved, as shown in Fig. 2f. These results suggest that the device has the potential for laser-tuned negative photoresponse properties. The device responsivity (R) as a function of the incident light power density (P) by fitting it with equation as:

$$R_{ph} = \frac{I_{ph}}{P_{in}S} \tag{1}$$

where $I_{ph} = I_{light} - I_{dark}$, P_{in} is the laser power density, and S is the active area of the phototransistor.[35,36] Fig. 2f and g show that the responsivity decreases and then gradually saturates as the power density increases. It has a maximum value of about 27.9 A W^{-1} at P_{in} = 7.0 mW cm^{-2}. The vertical WSe_2/CIPS heterostructure devices have the capability to convert light into electric signals and exhibit both positive photoresponse (positive ΔI_{ds}) and negative photoresponses (negative ΔI_{ds}), which are dependent on the gate voltage of preset-polarization. From Fig. 2h and i, we can observe that I_{gs} exhibits subtle fluctuations with variations in V_{ds}, indicative of its weak dependence on V_{ds}. However, with increasing laser intensity, I_{gs} demonstrates an upward trend. It is noteworthy that despite these variations, I_{gs} remains extremely smaller in magnitude compared to I_{ds}, highlighting the favorable characteristics of CIPS as a gate dielectric layer. Notably, Fig. 3a shows that by applying a positive gate voltage (V_{gs} = 2 V), the source/drain current experienced a significant decrease after exposure to light and gradually returned to its initial state once the illumination ceased, indicating the presence of the NPC effect. In contrast, PPC occurs for the applied a negative gate voltage (V_{gs} = −2 V) and without adding gate voltage (V_{gs} = 0 V), as shown in Fig. 3b and c.[24,37] The gray line in Fig. 3a and b reveals that I_{gs} remains relatively constant over time, and when juxtaposed with I_{ds}, its impact is almost negligible. These results are consistent with the trend of the output characteristic curve. In Fig. 3d–e, we analyze the response times of the WSe_2/CIPS heterostructure device with light. Notability, the mechanism of NPC is expected to cause a decay in photocurrent in a biexponential manner. Therefore, the photocurrent rise/decay characteristics at a time t under illumination could be fitted as:

$$I = I_0 + A_1 e^{-t/\tau_1} + A_2 e^{-t/\tau_2} \tag{2}$$

where I_0 represents the device current prior to the illumination with the fitting constants A_1 and A_2, and τ_1 and τ_2 represent the the fast and slow response components of the rise/decay edges, respectively.[38,39] The experimental results of the NPC phenomenon shows that two independent phenomena are responsible for the overall decrease in current under illumination. It is presumed that the smaller time constant (τ_1) is associated with rapid generation of trapped states, and then large time constants (τ_2) slow down the trapping process.[40] Fig. 3d suggests that the transient photoresponse of WSe_2/CIPS FeFET shows fast response with the rise time ($\tau_{r1} \approx$ 5.77s) and the decay time

 This journal is © The Royal Society of Chemistry 2023

Published on 30 August 2023. Downloaded by East China Normal University on 10/31/2023 1:35:46 AM.

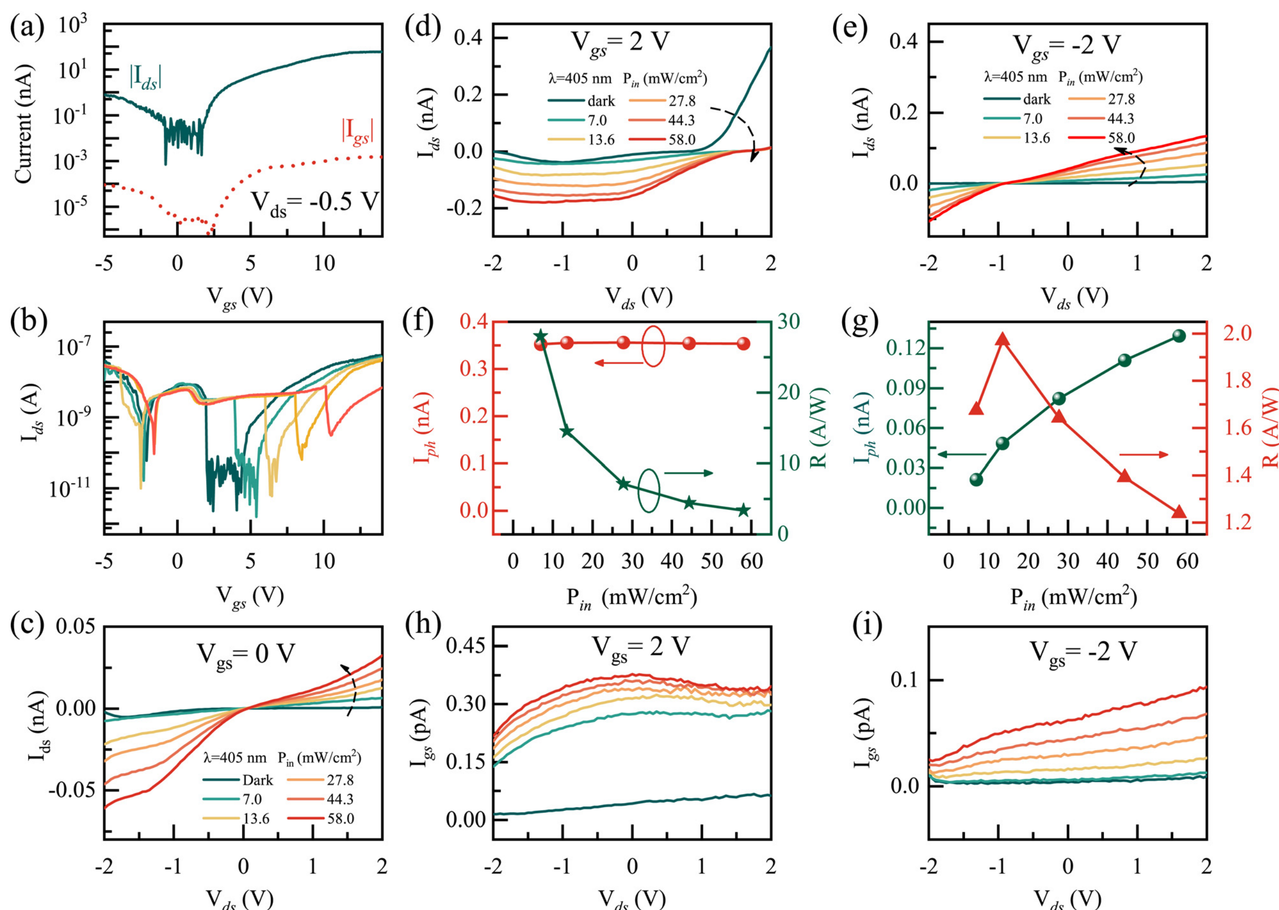

Fig. 2 WSe_2/CIPS heterostructure transistor characterization. (a) Transfer characteristic and gate leakage currents curve of WSe_2/CIPS heterostructure device were measured at V_{ds} = −0.5 V under dark condition. (b) Precise control of the V_{th} by timely controlling the turnoff of the light with the intensity of 7.0 mW cm^{-2} at V_{ds} = −0.5 V. Output characteristic curves of the device under the 405 nm laser with various laser power intensities at (c) V_{gs} = 0 V, (d) V_{gs} = 2 V, and (e) V_{gs} = −2 V, respectively. (f), (g) Responsivity and I_{ph} of the WSe_2/CIPS heterostructure device as a function of laser power density at V_{gs} = 2 V, and V_{gs} = −2 V. (h), (i) The correlation between V_{ds} and I_{gs} under the 405 nm laser with various laser power intensities at V_{gs} = 2 V and V_{gs} = −2 V, respectively.

(τ_{d1} ≈ 0.28 s), respectively, indicating the possibility of the device for high-speed photoelectronic response application. Moreover, for the case of V_{gs} = −2 V, the temporal response of the WSe_2/CIPS heterostructure device is given in Fig. 3e. In Fig. 3f, we can see the changes in light-induced current under different intensities. It is evident that the NPC phenomenon is closely related to the density of photo-generated electrons.

2.3. Working mechanism of WSe_2/CIPS heterostructure-based NPC

The characterization of the NPC effect is achieved insitu using the conductive atomic force microscope (C-AFM). The topographic image of the WSe_2/CIPS heterostructure is plotted in Fig. 4a. Fig. 4b shows the schematic diagram of the experimental configuration. The variable bias voltage was applied between the bottom Au layer electrode and the top electrode consisting of an AFM tip. At the nanoscale region, the voltage was directly applied to the WSe_2/CIPS heterostructure by the conductive tip to achieve electrical stimulation. An obvious sensing current is observed in certain regions when a bias voltage of 2 V is applied under dark. Fig. 4c–g show the C-AFM images of the CIPS/WSe_2 heterojunction at a gate voltage of 2 V under illumination with 405 nm laser. As the laser intensity increases, the photocurrent signal weakens, indicating the presence of photoinhibition insitu by the C-AFM. As shown in Fig. 4h, the average current of the WSe_2/CIPS heterostructure decreases with the light intensity increases. Specifically, when a laser with an intensity of 58 mW cm^{-2} is introduced, the photocurrent is nearly completely suppressed. *In situ* testing using C-AFM provides high-resolution current imaging, confirming the presence of the negative photoconductance effect in the WSe_2/CIPS heterostructure samples and investigating its relationship with light intensity. This reveals the charge migration and recombination processes on the sample surface under specific gate voltages under illumination.

To clarify the physical mechanism of the carrier transfer process with illumination modulated by the ferroelectric polarization of CIPS, the interface contact barriers were investigated. First, the band gap (∼1.6 eV and ∼2.87 eV) of bilayer WSe_2 and CIPS nanoflakes were calculated. Further, the top surface

Published on 30 August 2023. Downloaded by East China Normal University on 10/31/2023 1:35:46 AM.

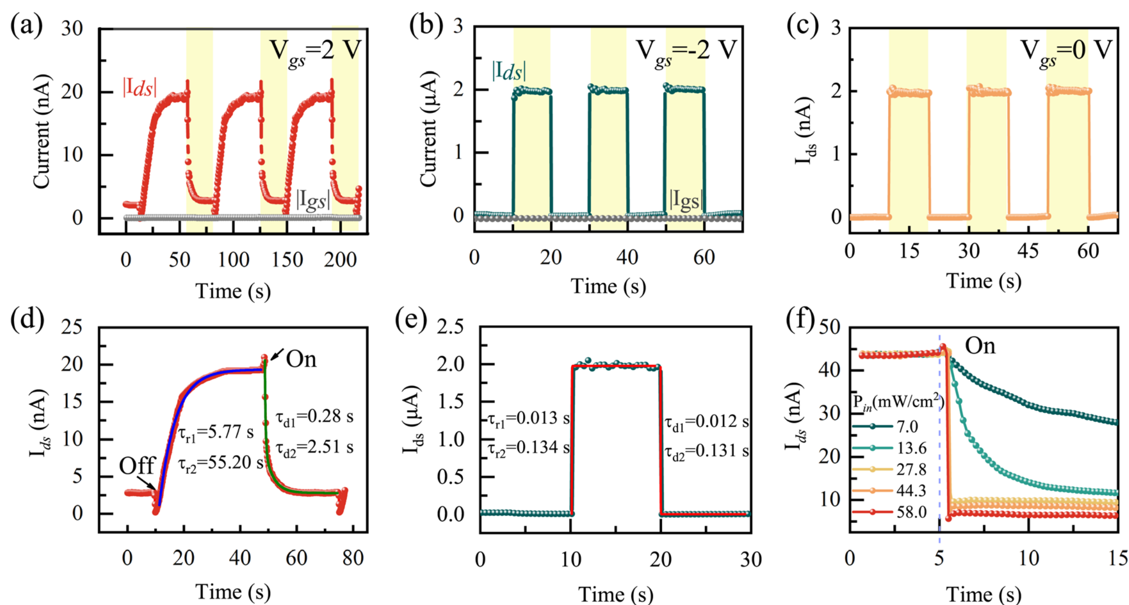

Fig. 3 Controllable and polarity-switchable photoresponse of WSe_2/CIPS heterostructure device. (a)–(c) Photoresponse of the WSe_2/CIPS heterostructure device at different preset gate voltages under UV light (405 nm) with incident light power of 7.0 mW cm^{-2}. (d)–(e) Response time characteristics of negative and positive photocurrent behavior of a single modulation cycle of the WSe_2/CIPS heterostructure. (f) Time-dependent current curves under different intensities of 405 nm wavelength.

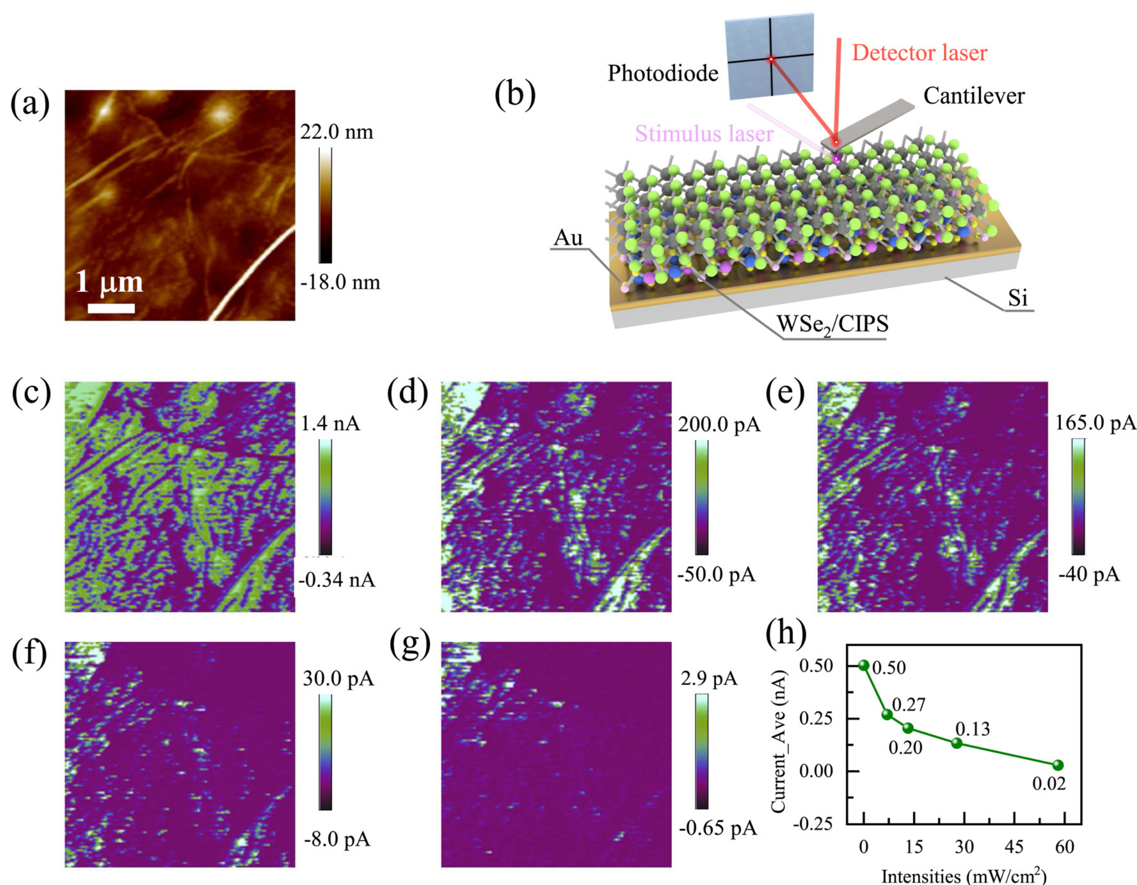

Fig. 4 (a) The AFM image of WSe_2/CIPS heterostructure. (b) Schematic diagram of the C-AFM measurement of the CIPS/WSe_2 hetrojunction. C-AFM image of the CIPS/WSe_2 hetrojunction at a gate voltage of 2 V of (c) under dark, (d) 7 mW cm^{-2}, (e) 13.2 mW cm^{-2}, (f) 27.8 mW cm^{-2}, and (g) 58 mW cm^{-2} illumination with 405 nm laser, respectively. (h) The average current over the tip-induced area on WSe_2/CIPS heterostructure.

 This journal is © The Royal Society of Chemistry 2023

Published on 30 August 2023. Downloaded by East China Normal University on 10/31/2023 1:35:46 AM.

potential of WSe_2/CIPS heterostructure regions with three polarization states was characterized by using Au substrate to calibrate the work function of AFM tip used in the Kelvin probe force microscopy (KPFM) test.[41] The surface potential difference of antiparallel OOP polarized domains with Au (the work function is 5.1 eV) is shown in Fig. 5a and b, which represents the Fermi level (EF) of the WSe_2/CIPS heterostructure modulated by the ferroelectric local electric field. Fig. 5b depicts the EF of the WSe_2/CIPS heterostructure P_{down} state is higher than that of the P_{up} state in the heterojunction interface before contacts. The electric field at the junction interface can be enhanced or inhibited by the ferroelectric field of CIPS, resulting in the accumulation or depletion of carriers. Additionally, the ferroelectric remanent polarization field, after reconstruction as shown in Fig. 5c, can modulate the barrier height (ϕ) across the junction and the electromotive force (EMF) as illuminated. The origin of the NPC phenomenon observed in the WSe_2/CIPS heterostructure can be elucidated by the coupling of built-in electric field with ferroelectric polarization and the charge transfer between the gate dielectric layer and the conduction channel.[21] Meantime, the schematic energy band diagram of conduction process are shown in Fig. 5d–f. When the WSe_2 and CIPS construct a heterojunction, the charge distribution is reconstructed, ensuring the dynamic balance of charge carriers at the heterojunction interface until the Fermi levels are aligned. Due to the relatively small energy gap of CIPS and WSe_2, the absorbed photons will generate electron–hole pairs under external light, which will be separated under the action of the built-in electric field and generate a current signal.[41] Fig. 5b shows that as a positive pre-polarization gate bias is applied, the total electric field in the junction area decreases, causing a decrease in I_{drift} and a current direction consistent with $I_{diffusion}$. This means that photo-generated holes on the CIPS side move to the junction area, and photo-generated electrons on the WSe_2 side move to the junction area. The photogenerated electrons and holes then meet and recombine with accumulated multi-holes and electrons spatially, resulting in a decrease in number of multi-carrier concentration in CIPS and WSe_2 layer, which eventually leads to the appearance of a negative photoelectric response. Conversely, when applying a negative pre polarization gate voltage, the junction current direction is the same as I_{drift}, meaning that photo-generated electrons on the CIPS side move to the junction region, and photo-generated holes on the WSe_2 side move to the junction region shown in Fig. 5f. It can result in an increase of multi-carrier concentration and conductivity for CIPS and WSe_2, generating a positive photoconductance signal.

2.4. DFT calculations of WSe_2/CIPS heterostructure

To confirm the physical mechanism of NPC phenomenon, the first-principle DFT calculations are provided to quantify the charge transfer to/from the WSe_2/CIPS heterostructure. We first performed band structure calculations for monolayer WSe_2 and CIPS. In Fig. 6a, WSe_2 exhibits a narrow direct band gap of 1.66 eV, with its the valence band maximum (VBM) and the conduction band minimum (CBM) located at the K point. Similarly, the CIPS has a wide direct band gap of 2.87 eV with its the VBM and the CBM located at point K, as shown in Fig. 6b, the band gap values of these two monolayers are in agreement with previously reported values. To check whether charge transfer occurs at the interface when the polarized states

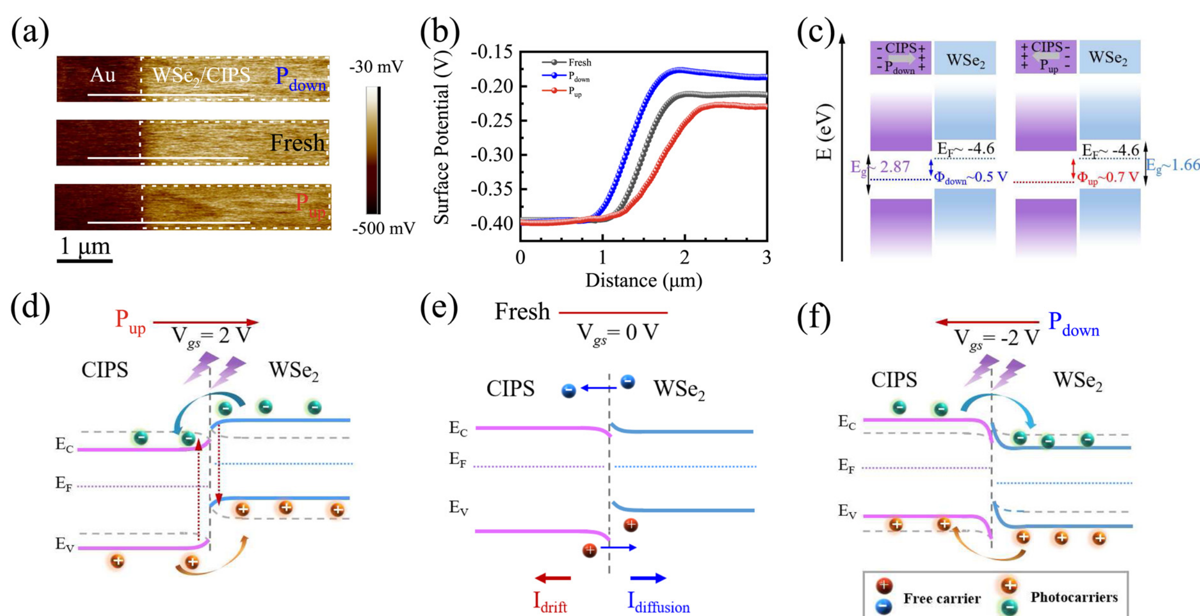

Fig. 5 Working mechanism of the WSe_2/CIPS heterostructure. (a) KPFM image of Au and WSe_2/CIPS heterostructure. (b) Surface potential between Au and WSe_2/CIPS heterostructure in three polarized states after poling *via* AFM conductive tip bias (±2 and 0 V). Surface potential profiles along with the corresponding cuts lines in (a). (c) Schematic of the band diagram of the WSe_2/CIPS heterojunction before contact. (d)–(f) Schematic energy band diagram of the mechanism of the polarity-switchable photoresponse under diverse polarization states (P_{up}, Fresh, and P_{down}).

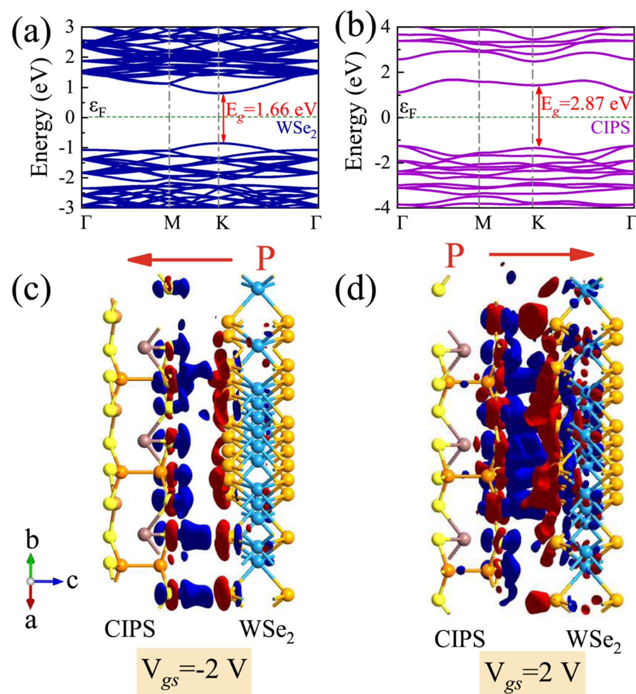

Fig. 6 DFT calculations using the HSE method based on first-principles calculations. (a) and (b) Energy band diagram of WSe_2. (b) Energy band diagram of CIPS. 3D isosurface of the charge density difference across the WSe_2/CIPS under different polarized states (c) V_{gs} = 2 V and (d) V_{gs} = −2 V, respectively. Red-colored isosurfaces show gain of charge, and blue-colored isosurfaces show loss of charge.

of WSe_2/CIPS heterostructure were modulated by the preset pulse, it is necessary to further investigate the charge redistribution with different polarized states. We constructed a WSe_2/CIPS heterostructure with monolayer of WSe_2 and monolayer of CIPS, Fig. 6c and d show the atomic models of WSe_2/CIPS heterostructure with two polarized states, along with the three-dimensional charge density difference diagrams at the side views, the red and blue indicate electron accumulation and depletion, respectively. The charge density is significantly rearranged at the interface and the electrons are transferred from WSe_2 to CIPS, indicating that the WSe_2/CIPS heterojunction trigger spontaneous electron diffusion. It should be noted that when V_{gs} = 2 V and V_{gs} = −2 V, the polarization direction is backwards and points to WSe_2, as demonstrated in Fig. 5c. In the case where the polarization direction points towards WSe_2, there is an evident increase in interfacial charge density, implying that the built-in electric field owing to polarization aligns with the direction of charge diffusion (Fig. 6c). The polarization field in CIPS facilitates the capture and recombination of photogenerated carrier at the heterostructure interface, which further confirms the possibility of NPC phenomenon. However, when the polarization in CIPS changes direction, as shown in Fig. 6d, the localized charge density becomes deconcentrated, and the junction current direction is opposite to the direction of charge diffusion. In this case, photo-generated electrons on the CIPS side move towards the junction region, promoting the separation of electron–hole pairs and the generation of PPC.

2.5 Potential application of WSe_2/CIPS heterostructure-based NPC

Experimental and theoretical investigations have revealed that phototransistors composed of WSe_2 and CIPS thin flakes exhibit distinct non-volatile conductivity adjustability, characterized by both PPC and NPC, under the synergistic effects of different pre-polarized gate voltages and optical stimulation within a single device. This intriguing feature positions the phototransistor as a fundamental building block in the design of secure optoelectronic encoders. While performing the encoding function, specific gate voltages and laser applications to individual phototransistors can serve as universal keys, enabling rapid optical encryption of any stored information corresponding to input encoding signals. Fig. 7a presents a schematic diagram of optical encryption and decryption process of a UV-light encoder. The initial electric signal generated from the signal generator is encrypted into a coded signal using a NPC encoder, and then the UV light is removed to decode the coded signal back into the original signal. As demonstrated in Fig. 7b, the eight cycles signals were respectively programmed to have the logic states of ''01000101'', ''01000011'', ''01001110'', and ''01010101'' reflecting the uppercase letters ''E'', ''C'', ''N'', and ''U'' according to the American Standard Code for Information Interchange (ASCII), respectively. From the transfer of the NPC under dark in Fig. 2a, it can be seen a clear difference in I_{ds} at V_{gs} = 0 V and V_{gs} = 3 V, which are utilized to represent these logic states based on the transistor's threshold voltage and characteristic behavior. At V_{gs} = 0 V, the transistor operates in a state where the channel is not effectively formed, resulting in a minimal I_{ds}. This low I_{ds} level is analogous to a logic state ''0'' in binary representation. Conversely, at V_{gs} = 3 V, the transistor enters a state where the channel is fully formed, leading to a higher I_{ds}. This increased I_{ds} level correlates with a logic state ''1'' in binary notation. Fig. 7c simulates the optical encryption process with current–time (I–t) dynamic response. The I_{ds} at V_{gs} = 0 V and V_{gs} = 3 V is utilized to represent the signal of ''0'' and ''1'' in dark conditions, respectively. After the introduction of ultraviolet light in the second cycle, all input signals become ''00000000'' attributed to the presence of negative photoelectric phenomenon at V_{gs} = 3 V, realizing the optical encryption of the original signal. Decoding is done by removing UV radiation. It decodes the scrambled signal back to the initial signal. Multilevel information encryption is essential for the development of secure information storage and anti-counterfeiting. Optical encryption with easy operation, multichannel and ultrahigh security provides a new way to the development of secure information storage and the security of signal transmission.[18] The potential implications of this finding are significant, as it offers exciting possibilities for secure data encryption and opens up avenues for exploring novel optoelectronic applications.

Published on 30 August 2023. Downloaded by East China Normal University on 10/31/2023 1:35:46 AM.

This journal is © The Royal Society of Chemistry 2023

View Article Online

Published on 30 August 2023. Downloaded by East China Normal University on 10/31/2023 1:35:46 AM.

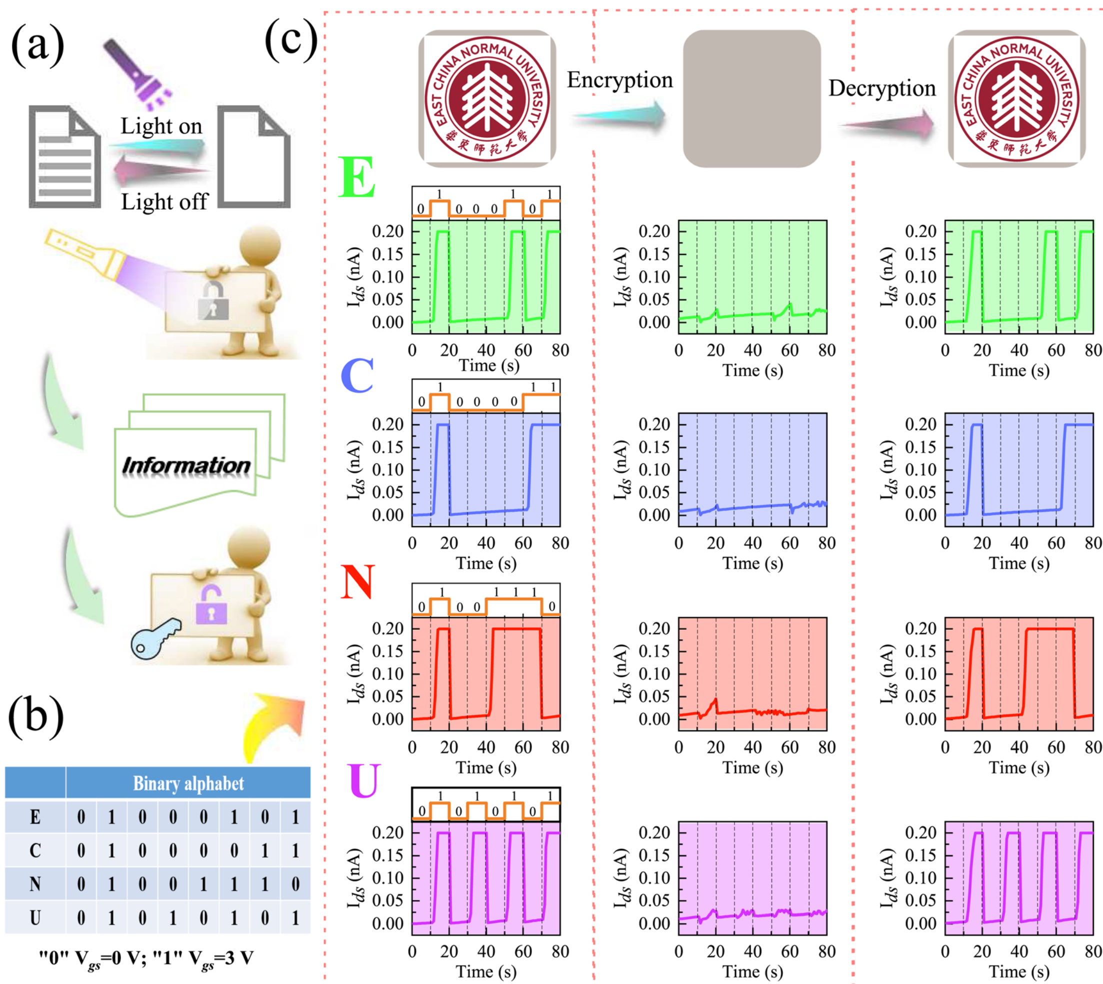

Fig. 7 Information encryption using NPC. (a) Schematic diagram of light encryption and decryption process of a UV-light encoder. (b) Uppercase letters of the "E", "C", "N", and "U" according to the binary alphabet. (c) Light encryption and decryption process of electrical signals of binary "E", "C", "N", and "U".

3 Conclusion

In summary, the study presents a novel approach in which we design a nonvolatile transistor based on a 2D WSe_2/CIPS heterostructure. By utilizing a specific gate voltage and laser as the encryption key, we successfully achieve the coexistence of controllable PPC and NPC in a single device. The unique switchable photoelectronic effect of WSe_2/CIPS heterostructure has been visualized *in situ* using the C-AFM system. Importantly, the process operates without a constant external voltage, indicating its potential for low power consumption. Based on the special photoconductive properties of the device structure, we realize the remarkable capability of light encryption within a single device. Furthermore, by controlling the light switch, we enable signal recovery and decryption, thereby establishing a controllable optical encryption function. This advancement holds significant implications for achieving high-security data storage and information encryption. Moreover, our findings provide an efficient strategy for designing NPC devices based on vdW low-dimensional materials. This breakthrough paves the way for the development of advanced and multifunctional optoelectronic applications.

4 Experimental section

4.1 Fabrication

The back gate, source, and drain electrodes (Cr/Au) were fabricated on heavily *n*-doped silicon wafers with 300 nm SiO_2 by electron beam lithography (EBL, Pioneer Two, Raith), metallization (thermal evaporation, Type-300, KONGMAILAI Co., Ltd), and the lift-off process. Low-dimensional CIPS and WSe_2 were mechanically exfoliated from the single crystals of bulk CIPS and WSe_2, were transferred onto the electrodes and formed the vertically stacked structure with the help of scotch tape and polydimethylsiloxane (PDMS).

4.2 Characterization

The surface morphology and thickness of CIPS and WSe_2 flakes were measured using a commercial atomic force

Published on 30 August 2023. Downloaded by East China Normal University on 10/31/2023 1:35:46 AM.

microscope (AFM) system (Dimension Icon, Bruker). Confocal micro-Raman spectrometer (Jobin-Yvon LabRAM HR Evolution, Horiba Jobin-Yvon) with the argon ion laser line of 532 nm was used to carry out the Raman and photoluminescence (PL) spectra. The crosssections of the WSe_2/CIPS heterostructures are prepared by a focused ion beam (FIB, GAIA3 GMU model 2016) for transmission electron microscopy (TEM, JEOL 2100F) observation. Beside, the absorption of the nanoflakes was recorded using a doube-beam UV-vis-NIR spectrophotometer (PerkinElmer Lambda 950). All electrical and photoresponse were measured at room temperature by a semiconductor parameter analyzer (4200-SCS, Keithley) under dark conditions, exposuring to the target light sources only. For the optoelectronic measurements, commercial light-emitting diodes with wavelengths of 405 nm (Thorlabs, Inc.) were employed. For the characterization of negative photoconductivity, the same 405 nm laser adopted in the lighting-TUNA measurements was used as the light source. A high vacuum with a pressure of 10^{-6} torr in the measurement chamber ensured the stability during the whole test process.

4.3 Density functional theory calculation

The optimization and electronic properties of heterostructures have been calculated based on the first-principles method of density functional theory (DFT), the calculations in this research were using the Atomistix ToolKit (ATK) software package.[42] The Kohn–Sham equations were solved using the state-of-the-art hybrid Heyd–Scuseria–Ernzerhof (HSE06) is used as the exchange correlation function, which is believed to provide a better description of the band structure.[43] The valence electronic state was expanded using a linear combination of atomic orbitals, and the basis function group was double ζ + polarization (DZP). The SG15 pseudopotential was used to calculate all atoms, and the Grimme DFT-D3 method was used to correct the van der Waals interaction between monlayers.[44,45] To optimize the structure, we used $9 \times 9 \times 1$ k-point sampling in the x, y, and z directions of the first Brillouin zone, while $11 \times 11 \times 1$ k-point sampling was used to calculate the electronic properties. The periodic directions of the heterostructure are x and y, while z is the vertical direction. To eliminate the interaction between the model and its "image", we set a vacuum layer greater than 25 in the aperiodic z orientation. The energy cut-off (Mesh cut-off) is uniformly set to 150 Ry. All calculations are based on the fact that the geometric model is optimized so that the force acting on each atom is less than 0.01 eV Å^{-1}, the stress between lattices is less than 0.01 GPa, and the total energy convergence standard is less than 10^{-5} eV per atom ongoing. At the same time, for the sake of simplicity, the Fermi level of the calculation results is set to zero.

Author contributions

A. Cao, H. Chen and Z. Hu initiated and designed the experiments and wrote the manuscript. A. Cao, S. Li, M. Deng, X. Xu and A. Cui gave sufficient discussions about C-AFM, KPFM and Raman data. A. Cao and S. Li conducted the experiments of device fabrication. H. Chen carried out the theoretical calculations. Y. Li, L. Shang and Z. Hu gave the detailed analysis of the underlying mechanism. All the authors contributed to the manuscript preparation.

Conflicts of interest

There are no conflicts to declare.

Acknowledgements

This work was financially supported by the National Key Research and Development Program of China (Grant No. 2019YFB2203403), the National Natural Science Foundation of China (Grant No. 62090013, 61974043, and 12104156), Projects of Science and Technology Commission of Shanghai Municipality (Grant No. 21JC1402100 and 23ZR1446400), the Natural Science Foundation of Chongqing, China (CSTB2022NSCQ-MSX1367), the Program for Professor of Special Appointment (Eastern Scholar) at Shanghai Institutions of Higher Learning.

References

1 F. Liu, L. You, K. L. Seyler, X. Li, P. Yu, J. Lin, X. Wang, J. Zhou, H. Wang and H. He, *Nat. Commun.*, 2016, **7**, 1–6.
2 F. Xue, W. Hu, K. C. Lee, L. S. Lu, J. Zhang, H. L. Tang, A. Han, W. T. Hsu, S. Tu and W. H. Chang, *Adv. Funct. Mater.*, 2018, **28**, 1803738.
3 Z. Fei, W. Zhao, T. A. Palomaki, B. Sun, M. K. Miller, Z. Zhao, J. Yan, X. Xu and D. H. Cobden, *Nature*, 2018, **560**, 336–339.
4 S. Yuan, X. Luo, H. L. Chan, C. Xiao, Y. Dai, M. Xie and J. Hao, *Nat. Commun.*, 2018, **10**(10), 1775.
5 M. Si, P. Y. Liao, G. Qiu, Y. Duan and P. D. Ye, *ACS Nano*, 2018, **12**, 6700–6705.
6 M. Zhao, G. Gou, X. Ding and J. Sun, *Nanoscale*, 2020, **12**, 12522–12530.
7 M. Si, A. K. Saha, P.-Y. Liao, S. Gao, S. M. Neumayer, J. Jian, J. Qin, N. B. Wisinger, H. Wang, P. Maksymovych, W. Wu, S. K. Gupta and P. D. Ye, *ACS Nano*, 2019, **13**, 8760–8765.
8 Z. Zhao, S. Rakheja and W. Zhu, *Nano Lett.*, 2021, **21**, 9318–9324.
9 L. Tu, R. Cao, X. Wang, Y. Chen, S. Wu, F. Wang, Z. Wang, H. Shen, T. Lin, P. Zhou, X. Meng, W. Hu, Q. Liu, J. Wang, M. Liu and J. Chu, *Nat. Commun.*, 2020, **11**(101), 6700–6705.
10 J. Y. Wu, Y. T. Chun, S. Li, T. Zhang, J. Wang, P. K. Shrestha and D. Chu, *Adv. Mater.*, 2018, **30**, 1705880.
11 A. De Oliveira, G. Ribeiro, D. Soares and H. Chacham, *Appl. Phys. Lett.*, 1994, **64**, 2258–2260.
12 Y. Yang, X. Peng, H.-S. Kim, T. Kim, S. Jeon, H. K. Kang, W. Choi, J. Song, Y.-J. Doh and D. Yu, *Nano Lett.*, 2015, **15**, 5875–5882.
13 X. Zhu, Y. Yan, L. Sun, Y. Ren, Y. Zhang, Y. Liu, X. Zhang, R. Li, H. Chen, J. Wu, F. Yang and W. Hu, *Adv. Mater.*, 2022, **34**, e2201364.

 This journal is © The Royal Society of Chemistry 2023

Published on 30 August 2023. Downloaded by East China Normal University on 10/31/2023 1:35:46 AM.

14 A. Grillo, E. Faella, A. Pelella, F. Giubileo, L. Ansari, F. Gity, P. K. Hurley, N. McEvoy and A. Di Bartolomeo, *Adv. Funct. Mater.*, 2021, **31**, 2105722.
15 S. Zhuang, Y. Chen, W. Zhang, Z. Chen and Z. Wang, *Sci. China: Phys., Mech. Astron.*, 2017, **61**, 1–6.
16 N. K. Tailor, P. Maity and S. Satapathi, *ACS Photon.*, 2021, **8**, 2473–2480.
17 N. K. Tailor, P. Maity, M. I. Saidaminov, N. Pradhan and S. Satapathi, *J. Phys. Chem. Lett.*, 2021, **12**, 2286–2292.
18 X. Zhu, Y. Yan, L. Sun, Y. Ren, Y. Zhang, Y. Liu, X. Zhang, R. Li, H. Chen and J. Wu, *Adv. Mater.*, 2022, **34**, 2201364.
19 C. Tan, R. Tao, Z. Yang, L. Yang, X. Huang, Y. Yang, F. Qi and Z. Wang, *Chin. Chem. Lett.*, 2023, **34**, 107979.
20 Z. Ye, C. Tan, X. Huang, Y. Ouyang, L. Yang, Z. Wang and M. Dong, *Nano-Micro Lett.*, 2023, **15**, 38.
21 Y. Wang, E. Liu, A. Gao, T. Cao, M. Long, C. Pan, L. Zhang, J. Zeng, C. Wang and W. Hu, *ACS Nano*, 2018, **12**, 9513–9520.
22 X. Wang, X. Zhou, A. Y. Cui, M. H. Deng, X. H. Xu, L. P. Xu, Y. Ye, K. Jiang, L. Y. Shang, L. Q. Zhu, J. Z. Zhang, Y. W. Li, Z. G. Hu and J. H. Chu, *Mater. Horiz.*, 2021, **8**, 1985–1997.
23 S. B. Li, M. Li, L. Chen, X. H. Xu, A. Y. Cui, X. Zhou, K. Jiang, L. Y. Shang, Y. W. Li, J. Z. Zhang, L. Q. Zhu, Z. G. Hu and J. H. Chu, *ACS Appl. Mater. Interfaces*, 2022, **14**, 45600–45610.
24 R. Wang, J. L. Wang, T. Liu, Z. He, H. Wang, J. W. Liu and S. H. Yu, *Adv. Mater.*, 2022, **34**, 2204698.
25 X. Jiang, X. Hu, J. Bian, K. Zhang, L. Chen, H. Zhu, Q. Sun and D. W. Zhang, *ACS Appl. Electron. Mater.*, 2021, **3**, 4711–4717.
26 M. Si, A. K. Saha, P.-Y. Liao, S. Gao, S. M. Neumayer, J. Jian, J. Qin, N. Balke Wisinger, H. Wang and P. Maksymovych, *ACS Nano*, 2019, **13**, 8760–8765.
27 P. Li, A. Chaturvedi, H. Zhou, G. Zhang, Q. Li, J. Xue, Z. Zhou, S. Wang, K. Zhou and Y. Weng, *Adv. Funct. Mater.*, 2022, **32**, 2201359.
28 J. Wu, H.-Y. Chen, N. Yang, J. Cao, X. Yan, F. Liu, Q. Sun, X. Ling, J. Guo and H. Wang, *Nat. Electron.*, 2020, **3**, 466–472.
29 B. Li, S. Li, H. Wang, L. Chen, L. Liu, X. Feng, Y. Li, J. Chen, X. Gong and K. W. Ang, *Adv. Electron. Mater.*, 2020, **6**, 2000760.
30 Y. Huang, C. Zhao, S. Zhong and J. Wu, *Acta Mater.*, 2021, **209**, 116792.
31 M. Si, P.-Y. Liao, G. Qiu, Y. Duan and P. D. Ye, *ACS Nano*, 2018, **12**, 6700–6705.
32 J. Wu, H.-Y. Chen, N. Yang, J. Cao, X. Yan, F. Liu, Q. Sun, X. Ling, J. Guo and H. Wang, *Nat. Electron.*, 2020, **3**, 466–472.
33 Y. S. Kim, S. Kang, J.-P. So, J. C. Kim, K. Kim, S. Yang, Y. Jung, Y. Shin, S. Lee and D. Lee, *Sci. Adv.*, 2021, **7**, eabd7921.
34 P. Meng, Y. Wu, R. Bian, E. Pan, B. Dong, X. Zhao, J. Chen, L. Wu, Y. Sun and Q. Fu, *Nat. Commun.*, 2022, **13**, 7696.
35 K. Xu, Y. Huang, B. Chen, Y. Xia, W. Lei, Z. Wang, Q. Wang, F. Wang, L. Yin and J. He, *Small*, 2016, **12**, 3106–3111.
36 J. Kim, K. Cho, J. Pak, W. Lee, J. Seo, J.-K. Kim, J. Shin, J. Jang, K.-Y. Baek and J. Lee, *ACS Nano*, 2022, **16**, 5376–5383.
37 C. Y. Wang, S. J. Liang, S. Wang, P. Wang, Z. A. Li, Z. Wang, A. Gao, C. Pan, C. Liu and J. Liu, *Sci. Adv.*, 2020, **6**, eaba6173.
38 K. Li, T. He, N. Guo, T. Xu, X. Fu, F. Wang, H. Xu, G. Li, S. Liu and K. Deng, *Adv. Opt. Mater.*, 2023, **11**, 2202379.
39 X. Zhou, M. Li, J. Z. Zhang, L. Y. Shang, K. Jiang, Y. W. Li, L. Q. Zhu, J. H. Chu and Z. G. Hu, *IEEE Electron Device Lett.*, 2022, **43**, 1921–1924.
40 S. Paramanik and A. J. Pal, *Nanoscale*, 2023, **15**, 5001–5010.
41 C. Jia, S. Wu, J. Fan, C. Luo, M. Fan, M. Li, L. He, Y. Yang and H. Zhang, *ACS Nano*, 2023, **17**, 6534–6544.
42 Z. Dan, B. Yang, Q. Song, J. Chen, H. Li, W. Gao, L. Huang, M. Zhang, M. Yang, Z. Zheng, N. Huo, L. Han and J. Li, *ACS Appl. Mater. Interfaces*, 2023, **15**, 18101–18113.
43 C. Q. Nguyen, Y. S. Ang, S.-T. Nguyen, N. V. Hoang, N. M. Hung and C. V. Nguyen, *Phys. Rev. B*, 2022, **105**, 045303.
44 A. Grillo, E. Faella, A. Pelella, F. Giubileo, L. Ansari, F. Gity, P. K. Hurley, N. McEvoy and A. Di Bartolomeo, *Adv. Funct. Mater.*, 2021, **31**, 2105722.
45 Q. Zhou, X. Qiu, X. Su, Q. Liu, Y. Wen, M. Xu and F. Li, *Small*, 2021, **17**, e2100377.